



HAL
open science

Strong electronic winds blowing under liquid flows on carbon surfaces

Mathieu Lizée, Alice Marcotte, Baptiste Coquinot, Nikita Kavokine, Karen Sobnath, Clément Barraud, Ankit Bhardwaj, Boya Radha, Antoine Niguès, Lydéric Bocquet, et al.

► **To cite this version:**

Mathieu Lizée, Alice Marcotte, Baptiste Coquinot, Nikita Kavokine, Karen Sobnath, et al.. Strong electronic winds blowing under liquid flows on carbon surfaces. *Physical Review X*, 2023, 13 (1), pp.011020. 10.1103/PhysRevX.13.011020. hal-03665101v2

HAL Id: hal-03665101

<https://hal.science/hal-03665101v2>

Submitted on 11 May 2022 (v2), last revised 3 Sep 2024 (v3)

HAL is a multi-disciplinary open access archive for the deposit and dissemination of scientific research documents, whether they are published or not. The documents may come from teaching and research institutions in France or abroad, or from public or private research centers.

L'archive ouverte pluridisciplinaire **HAL**, est destinée au dépôt et à la diffusion de documents scientifiques de niveau recherche, publiés ou non, émanant des établissements d'enseignement et de recherche français ou étrangers, des laboratoires publics ou privés.



Distributed under a Creative Commons Attribution 4.0 International License

Strong electronic winds blowing under liquid flows on carbon surfaces

Alice Marcotte^{†,1} Mathieu Lizee^{†,1} Baptiste Coquinot,^{1,2} Nikita Kavokine,² Karen Sobnath,³ Clément Barraud,³ Ankit Bhardwaj,^{4,5} Boya Radha,^{4,5} Antoine Niguès,¹ Lydéric Bocquet,¹ and Alessandro Siria¹

¹*Laboratoire de Physique de l'École Normale Supérieure,
ENS, Université PSL, CNRS, 3 Sorbonne Université,
Université Paris Cité, 75005 Paris, France*

²*Center for Computational Quantum Physics, Flatiron Institute, New York, USA*

³*Université Paris Cité, Laboratoire Matériaux et Phénomènes Quantiques, CNRS, F-75013 Paris, France*

⁴*National Graphene Institute, The University of Manchester, UK*

⁵*Department of Physics and Astronomy, The University of Manchester, UK*

The interface between a liquid and a solid is the location of plethora of intricate mechanisms at the nanoscale, at the root of their specific emerging properties in natural processes or technological applications [1, 2]. However, while the structural properties and chemistry of interfaces have been intensively explored, the effect of the solid-state electronic transport at the fluid interface has been broadly overlooked up to now. It has been reported that water flowing against carbon-based nanomaterials, such as carbon nanotubes [3–8] or graphene sheets [9–14], does induce electronic currents, but the mechanism at stake remains controversial [9, 10, 15]. Here, we unveil the molecular mechanisms underlying the hydro-electronic couplings by investigating the electronic conversion under flow at the nanoscale. We use a tuning fork-Atomic Force Microscope (AFM) to deposit and displace a micrometric droplet of both ionic and non-ionic liquids on a multilayer graphene sample, while recording the electrical current across the carbon flake. We report measurements of an oscillation-induced current which is several orders of magnitude larger than previously reported for water on carbon [13], and further boosted by the presence of surface wrinkles on the carbon layer. Our results point to a peculiar momentum transfer mechanism between fluid molecules and charge carriers in the carbon walls mediated by phonon excitations in the solid [3, 11]. Our findings pave the way for active control of fluid transfer at the nanoscale by harnessing the complex interplay between collective excitations in the solid and the molecules in the fluid.

Transport of fluid across or at the interface of carbon unveiled unexpected properties in term of very fast permeation, non-linear ionic transport and sieving and even energy storage and harnessing [2]. These results highlight the subtle interactions of water and charges with the carbon surface. Classically, the interaction of a fluid with a solid wall is based on picturing the solid as a static periodic potential that acts on the fluid molecules: interactions result from collisions on the surface roughness, as flows induced on the roughness scale dissipate mechanical energy. However, recent results for fluid and ion transport in carbon nanotubes and nanochannels made of graphitic materials have pointed out the limits of such standard description for fluid-solid interactions and existing couplings of liquid transport with electronic degrees of freedom inside the confining walls. This takes the form of electronic currents induced in the solid surface under flowing

liquid [4, 5, 7–14], the modification of wetting by electronic screening [16, 17], or anomalies in the water-carbon friction [18]. The interaction mechanisms at stake remain largely unexplained and to be properly understood.

In this article, we report the generation of electric current in a few-layer graphene sample by the displacement of a sub-micrometer scale liquid droplet along its surface. We deposited a thin graphite flake (1 to 70 nm in thickness) onto a Si/SiO₂ substrate; two gold electrodes, separated by a distance of $\sim 10\mu\text{m}$ and connected to a low noise current amplifier, allowed us to measure the electric current passing through the flake (see Figure S1). The sample was placed in a tuning fork atomic force microscope (AFM), that was specifically designed for controlled liquid deposition, see Figure 1a. The liquid was introduced into a quartz capillary, which was then glued to the quartz tuning fork (see Figure S2). A piezo-dither induced a nanometric oscillation of the tuning fork at its resonant frequency ($f_0 \approx 32\text{ kHz}$), a typical resonance curve is shown in the inset of Figure 1a. By monitoring precisely the tuning

[†] These authors contributed equally to this work

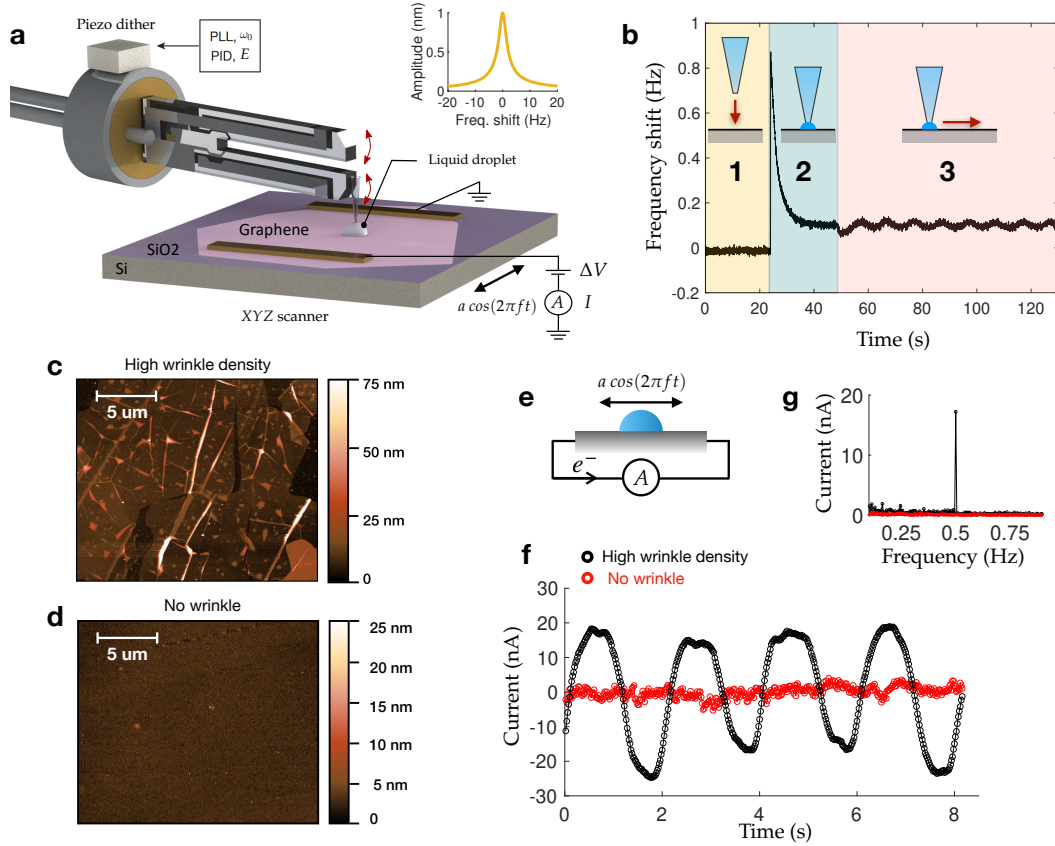


Figure 1: **Experimental set-up.** **a**, Schematic of the experiment. A quartz capillary of tip diameter of 500 nm is filled with liquid and glued on the lower prong of a millimetric quartz tuning fork. Once the tip is in contact with the graphite substrate, a liquid droplet is formed at its extremity. The scanner allows for droplet relative motion on the graphite flake in the XY-plane, while current is measured between both gold electrodes. An additional electric potential drop ΔV can be imposed between the electrodes. *Inset*: The resonance curve of the tuning fork whose frequency shift is used to deposit the droplet and maintain a gentle mechanical contact. **b**, Frequency shift response of the AFM during a typical experiment, indicating the stiffness of the pipette-sample contact. First, the pipette is brought into contact with the sample (1). After the contact, a slow relaxation (2) indicates the formation of the droplet. Finally, the sample is put into horizontal motion with respect to the droplet while a PID controller keeps a constant frequency shift (3). **c**, AFM image of a multilayer graphene sample (3.6 nm thick) exhibiting a high density of wrinkles. **d**, AFM image of a flat multilayer graphene sample (1.5 nm-thick). **e**, Schematic of droplet motion. **f**, Current (nA) as a function of time (s) resulting from droplet oscillations of 2 μm amplitude and 0.5 Hz frequency, on the wrinkled sample displayed on **c** (black dots) and on the flat graphite sample displayed on **d** (red dots). **g**, The corresponding current spectra as a function of frequency. For the wrinkled sample (black curve), the spectrum displays a peak at the droplet oscillation frequency (0.5 Hz).

fork oscillation's phase and amplitude as the pipette tip approach the sample, we achieved a fully controlled contact between the carbon surface and the pipette's aperture, leading to the formation of a liquid capillary bridge. The capillary bridge then evolved into a droplet, of radius fixed by the outer diameter of the tip (500 nm) [19, 20]. This novel experimental set-

up allows to deposit very viscous liquid at nano and micro scale over a broad range of substrates [21]. We used a room temperature ionic liquid (BMIM-PF6) and a neutral and apolar silicon oil (Polyphenyl-methylsiloxane), both very viscous with a viscosity of 0.3 Pa·s and 0.1 Pa·s, respectively, and with very small vapor pressures, allowing us to safely neglect evaporation. The

continuous monitoring of the contact with both the in-situ optical microscope and the AFM frequency shift signal allows us to ensure that the droplet remained hooked to the tip, sliding over the carbon surface. Moreover, motion does preserve the roughly spherical shape of the droplet (see Figure S2d).

In a typical experiment, the droplet is put into oscillatory motion along the carbon surface by a piezo-scanner with an amplitude of a few microns at a frequency of the order of 1 Hz. An electric current through the carbon surface is then measured at the droplet oscillation frequency (Figure 1e and Figure S3). As shown on Figure 1a, our set-up enables to further impose a constant potential drop ΔV (typically between -50 mV and 50 mV) between the electrodes. We report electric currents in the tens of nano-Ampere range induced by a droplet moving at a few micrometers per second. To allow for a comparison with other current generation experiments, we define the current density as the AC-current amplitude divided by the diameter of the droplet (of order $1\mu\text{m}$): $j = I/(2R_{\text{drop}})$ typically in the tens of $\text{nA}/\mu\text{m}$ range.

Firstly, several benchmark measurements allowed us to ensure that the current generation is due to the specific interaction of the liquid droplet with the few-layer graphene. We checked that no alternating current is recorded when the deposited droplet oscillates over the SiO_2 substrate between the electrodes but without the multilayer graphene substrate. We further controlled that no current is generated when the pipette is not in contact with the graphite but slightly above or even when a tungsten tip is used instead of the liquid filled pipette, see Figure S4. Altogether, we can safely conclude that the measured effect is due to the displacement of the liquid droplet on the carbon surface.

On Figure 2a, we report results of several samples (with thickness varying between 1.7 and 8.2 nm), where an electro-fluidic current is measured. We observe that for a fixed oscillation frequency f and bias voltage ΔV , the amplitude of the AC generated current increases linearly with the droplet oscillation amplitude a , or equivalently, with the droplet peak velocity ($v = 2\pi fa$). Taking advantage of the demonstrated linear dependency of the current density with respect to the droplet peak velocity, we define the electro-fluidic conductivity of our samples as

$$\sigma_{\text{ef}} = \frac{j}{v},$$

quantifying the cross-coupling between electronic current j and liquid flow v . Among the five samples presented here, we show an electro-fluidic conductivity ranging from 2.8 to 21.6 $\text{nA.s}/\mu\text{m}^2$ for a droplet size in the micrometer range.

To understand the mechanism driving this electro-fluidic current and having in mind the strongly energy-dependent electronic density of graphene close to the Fermi level [22], we tune the bias voltage ΔV between the electrodes and measure its influence on the electro-fluidic current. We show that the alternating current induced by the droplet oscillation strongly depends on ΔV , with a linear dependency. This is highlighted in Figures 2b-c, where the electro-fluidic conductivity is shown to scale roughly linearly with the potential drop ΔV , with a small or negligible shift at zero potential drop and a sign reversal of the current for negative versus positive ΔV . Finally, the slope of this linear dependency $\sigma_{\text{ef}}/\Delta V$ is in the range of 0.05 to 0.2 $\text{nA.s}/\mu\text{m}^2/\text{mV}$, see Figure 2c, and slightly varies across samples.

Now, an unexpected feature of the experimental results is the sharp distinction among carbon samples regarding the amplitude of the electro-fluidic conductivity. Over all few-layer-graphene measured, with thicknesses ranging from 1 nm up to 70 nm, we observe that the thinner ones tends to exhibit the largest electro-fluidic conductivity, see Figure S7a. However, investigating the surface topography of the carbon samples using AFM imaging, such as on Figure 1c-d, we rather reveal a correlation between the amplitude of the electro-fluidic conductivity and the existence of surface corrugation in the forms of folds and wrinkles. Notably, thinner samples exhibit a large number of folds and wrinkles whereas thicker samples present a flat surface without folds or defects (see Figure S1). This difference is due to the fabrication process involving the transfer of the exfoliated graphene flake onto the oxidized silicon wafer (See Sec. S-I) : the thinner flakes are softer and more flexible than the thicker ones, and more likely to exhibit wrinkles [23, 24], see Figure 1a and Figure S7. In order to disentangle the role of wrinkles from that of sample thickness, we implemented an alternative fabrication method in which all transfer steps are avoided and few-layer graphene flakes were directly exfoliated on the Si/SiO₂ wafer. This allowed us to obtain sub-10 nm, un-transferred and *smooth* graphene samples with a uniform wrinkle-free surface (see Figure 1b and Figure S1) to compare with the *transferred* and *crumpled* flakes of similar thick-

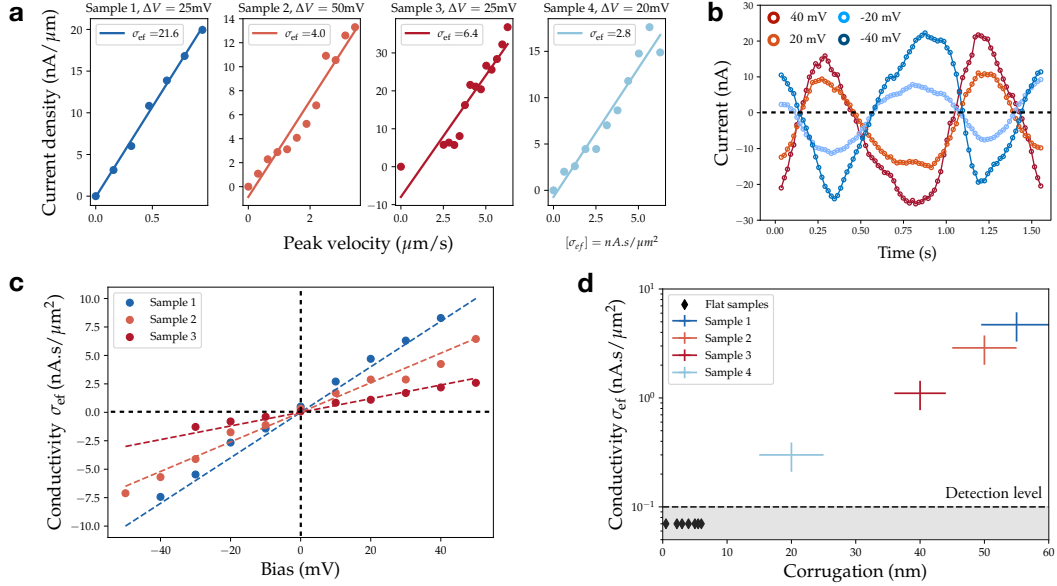


Figure 2: **Generation of a droplet motion-induced electronic current.** **a**, Current density (nA/ μm) as a function of fluid velocity $v = 2\pi fa$ for 4 different samples. Each curve is measured at a bias ΔV indicated in the corresponding plot. The multi-layer graphene substrates have thickness 3.3, 1.7, 3.6 and 8.2nm, respectively and their corresponding surface roughness measured using AFM are [55,50,40,20] nm respectively. **b**, Time-dependent current under droplet oscillation for various voltage bias ΔV . **c**, Effect of the voltage bias ΔV on the electro-fluidic conductivity $\sigma_{\text{ef}} = j/v$, showing a linear dependency. The dotted lines are guides to the eye. **d**, Electro-fluidic conductivity σ_{ef} (at $\Delta V = 20\text{mV}$) versus the substrate corrugation, measured using AFM images. The black diamonds correspond to current measurements below the detection level.

ness showing a much larger surface corrugation (see Figure S9 for a Raman analysis of wrinkles). As shown on Figure 2d, droplet motion on smooth samples results in no detectable current. *A contrario*, crumpled flakes of the same thickness have a high wrinkle density and show the strongest electro-fluidic conductivity, in the nA.s/ μm^2 range. Our results reveal that wrinkles are instrumental to the current generation mechanism, while there is no evidence of an effect of graphene thickness. Further evidence of the crucial role of wrinkles is provided by the dependence of the generated current on the droplet oscillation direction, see Figure S8. As expected, the current amplitude is 180° periodic with respect to the angle between the droplet trajectory and the electrodes. However, the maximal amplitude is not necessarily reached when the droplet oscillation is perpendicular to the electrodes, and the direction yielding the maximum current strongly depends on the position on the sample’s surface. We argue that this spatial and directional variability is related to the random distribution in height,

position and direction of the wrinkles on the carbon surface. This further highlights the role of wrinkles as current amplifiers. Let us note for completeness that the data displayed on Figure 2 are obtained along the direction with maximal amplitude.

Summarizing our experimental results, we have shown that the motion of a micrometric droplet on a crumpled, few-layer graphene surface generates a strong electro-fluidic current in the flake, which is proportional to the velocity of the droplet, as well as to the bias voltage applied between the electrodes. A remarkable feature is the strong dependence of the magnitude of the generated current on the surface corrugation of the flake.

While our results echo previous reports of electric potential differences induced by water flow in carbon-based nanomaterials [3–14], our nanoscale investigation puts us in position to disentangle various effects at the root of electronic current generation under fluid flow, and get much insights into the molecular mechanism underlying the phenomenon. Previously, sev-

eral mechanisms have been invoked to rationalize such conversion, including streaming potential effects [5], adsorbed/desorbed ion hopping [6, 9], Coulomb drag [4, 8] or charging/discharging of a pseudo-capacitance [13, 14]. These mechanisms involve Coulomb interactions between the polar liquid – exhibiting molecular partial charges – and the carbon surface as the main pathway for momentum transfer from the liquid to the electrons. As we now show, these previous explanations fail to account for the phenomenon at stake. Indeed, the strong effect of surface corrugation reported here suggests that current generation proceeds through a ‘mechanical’ transfer of momentum of the fluid towards the electronic degrees of freedom. In order to confirm this hypothesis and rule out any effect caused by the charges in the ionic liquid, we first repeated the experiment, now with an apolar silicone oil replacing the ionic liquid (and a wrinkled few-layer graphene as a substrate). We do observe qualitatively and quantitatively similar current generation for the silicone oil and the ionic liquid, see Figure S5. This discards coulombic couplings between the liquid molecules and the electrons and all corresponding mechanisms based on charge-charge interactions across the interface. These considerations naturally lead us to reconsider phonon-drag mechanisms, as first proposed theoretically in 2001 [3] as the driving mechanism for the measured electro-fluidic current. The phonon drag relies on hydrodynamic (viscous) friction at the solid-liquid interface, which transfers momentum to the solid’s phonons, thereby exciting a ‘phonon wind’. Through the electron-phonon interaction, the phonon wind ‘blows’ on the Fermi sea, so that electrons near the Fermi surface are dragged along the direction of the liquid flow, hence producing an electric current (see Figure 3a). A complete theory of phonon drag at the quantum level, within the non-equilibrium Keldysh framework is developed in [25]. Here, we give only a semi quantitative description that allows us to capture the main physical ingredients.

First, assuming a Couette flow within the liquid droplet, the hydrodynamic friction force is $\mathbf{F}_0 \sim \eta \mathcal{A}_{\text{drop}} \mathbf{v}_{\text{drop}} / h_{\text{drop}}$, v_{drop} is the drop velocity, η its viscosity, $\mathcal{A}_{\text{drop}}$ its surface and h_{drop} its height (here typically, $\eta = 0.3 \text{ Pa} \cdot \text{s}$ and $h_{\text{drop}} \approx 1 \mu\text{m}$). In line with observations, wrinkles are expected to enhance this hydrodynamics friction force. In a simple picture, wrinkles are modelled as protusions on which the flowing liquid exerts a Stokes force scaling (per wrinkle) as $\mathbf{F}_W \propto \eta h_W \mathbf{v}_{\text{drop}}$, where h_W is the typical height of the wrinkles ($h_W \sim 10 - 30 \text{ nm}$).

One then obtains a total friction force $\mathbf{F}_W \sim \mathbf{F}_0(1+W)$, where we introduced the dimensionless wrinkling number, $W = 3\pi n_W h_W h_{\text{drop}}$, with n_W the wrinkle density to account for the increase in viscous friction due to surface corrugation.

Our model is sketched on Figure 3a-d : the hydrodynamic friction force transfers momentum from the liquid (Figure 3a) to the solid exciting acoustic phonons with dispersion relation $\epsilon_{\mathbf{q}} = \hbar qc$ where c is the phonon (sound) velocity ($c \approx 2 \times 10^4 \text{ m} \cdot \text{s}^{-1}$ [26, 28, 29]). The phonons are mainly relaxed by transferring their momentum to the crystal (Figure 3d) through Umklapp processes [26], on a typical timescale $\tau_{\text{um}} \sim 10 \text{ ps}$ [27]. As sketched on Figure 3b, the constant influx of momentum modifies the phononic distribution by shifting the energetic cost of a phonon of wavevector \mathbf{q} according to $\epsilon_{\mathbf{q}} \mapsto \epsilon_{\mathbf{q}} - \hbar \mathbf{q} \cdot \mathbf{v}_{\text{eff}}$, which is lower along the direction of the liquid flow. Here \mathbf{v}_{eff} is the effective velocity of the phonon wind: it is determined by balancing the momentum fluxes in and out of the phonon system, according to $\tau_{\text{um}} \mathbf{F}_W / \mathcal{A}_{\text{drop}} = \Delta \mathbf{P}_{\text{ph}} / \mathcal{A}_{\text{drop}} = \int \frac{d\mathbf{q}}{2\pi} \hbar \mathbf{q} n_{\text{B}} (\hbar qc - \hbar \mathbf{q} \cdot \mathbf{v}_{\text{eff}})$, with n_{B} the Bose-Einstein distribution and \mathbf{q} is the phonon wavevector, that we assume two-dimensional. This yields

$$\mathbf{v}_{\text{eff}} \simeq \frac{2\pi}{3\zeta(3)} \frac{\hbar^2 c^4}{(k_{\text{B}} T)^3} \times (1+W) \eta \frac{\mathbf{v}_{\text{drop}}}{h_{\text{drop}}} \times \tau_{\text{um}} \quad (1)$$

Then, $v_{\text{eff}} \approx 9 \cdot 10^4 \times (1+W) \times v_{\text{drop}}$. As the electrons scatter on the phonons, they acquire an average velocity equal to the phonon wind velocity; our complete theory shows that this is true whatever the form of the electron-phonon interaction [25]. As sketched on Figure 3c, in a 2d model of the solid, this amounts to shifting the band energies according to $\epsilon_{\mathbf{q}} \mapsto \epsilon_{\mathbf{q}} - \hbar \mathbf{q} \cdot \mathbf{v}_{\text{eff}}$. Assuming for concreteness that the liquid flows to the right, this roughly means that in an energy window of width $\hbar k_{\text{F}} v_{\text{eff}}$ around the Fermi level (k_{F} is the Fermi wavevector), the electrons move to the right at the Fermi velocity v_{F} . The corresponding current density reads

$$\mathbf{j} = e v_{\text{F}} \times N(\epsilon_{\text{F}}) \times [\hbar k_{\text{F}} \mathbf{v}_{\text{eff}}], \quad (2)$$

where $N(\epsilon_{\text{F}})$ is the density of states at the Fermi level ϵ_{F} . We obtain a current density proportional to the droplet velocity, to the liquid viscosity and to the wrinkling number W in excellent agreement with the experiment. Moreover, the current is independent of the chemical nature of the liquid as observed in experiment (ionic liquid and silicone oil generate similar

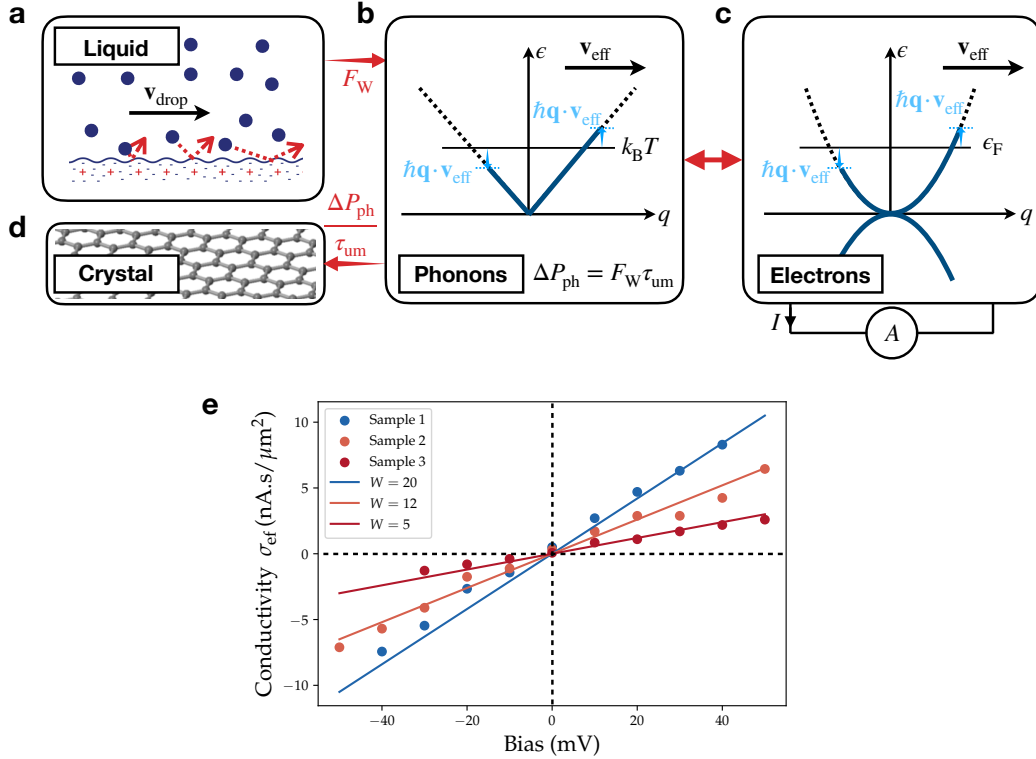


Figure 3: **Phonon drag mechanism.** The flowing liquid **a** exerts a friction force F_W on the graphite sample. This force is related to a momentum transfer to the phonons, that generates an asymmetry in the phonon distribution **b** which is biased in the direction of the liquid flow.

Finally this asymmetry propagates to the electronic distribution **c** by electron-phonon interaction. This asymmetry in the electronic distribution translates into the generation of a net electric current, whose sign depends on the nature of charge carriers at the Fermi level (electrons or holes). We stress that this is an out of equilibrium phenomenon in which most of the momentum is relaxed to the crystal **d** by the Umklapp process with a rate $1/\tau_{um}$. Finally, on **e**, we compare the theoretical derivation of the electro-fluidic conductivity σ_{ef} versus the bias voltage ΔV . We stress that the experimental data is the same as in Figure 2c and that the solid lines are plotted using Eq. (4) assuming the bulk graphite effective mass $m = 0.1m_e$ and W the wrinkling number as the only fitting parameter chosen between 5 and 20. This wrinkling number characterizes the enhancement of Stokes friction due to wrinkles on the graphene surface.

current). According to the complete derivation presented in [25] (see Sec. S-III for the main ingredients), we add in the following a correction factor of order 1/2 to the current density.

Electronic bands in graphene have a linear dispersion, $\epsilon_q = \hbar v_F q$; however, in our multilayer samples of few-nanometer thickness (see Figure S7a) one expects the electronic properties to be better described by a parabolic band with effective mass m [30–32]: $\epsilon_q = \hbar^2 q^2 / 2m$. The density of states is then independent of energy: $N(\epsilon) = N(\epsilon_F) = m/\hbar^2$. Altogether, we obtain the electro-fluidic cross conductivity

$$\sigma_{ef} = e \frac{m}{\hbar^2} \epsilon_F \times \frac{v_{eff}}{v_{drop}}. \quad (3)$$

The prediction in Eq. (3) can now be compared with experimental results. Experimentally, the applied bias voltage, sets the Fermi level $\epsilon_F \approx e\Delta V/2$, so that

$$\sigma_{ef} \approx 0.1 \times m/m_e \times (1 + W) \times \Delta V \text{ [nA.s}/\mu\text{m}^2] \quad (4)$$

with ΔV in mV. This estimate quantitatively reproduces the conductivity measured experimentally of a few nA.s/ μm^2 with the correct linear scalings of the electro-fluidic conductivity with the droplet velocity and the bias voltage. In addition, this current is proportional to the wrinkling number, in line with the observed impact of the presence of surface wrinkles as current amplifiers. On Figure 3e, we compare

this theoretical prediction with the experimental measurement of σ_{ef} as a function of the bias voltage. For the electronic effective mass, we consider graphite in a parabolic approximation, $m \sim 0.1m_e$, where m_e is the electron mass [30]. The theoretical estimate involves no fitting parameter other than the wrinkling number W chosen between 5 and 20 to reproduce the experimental data.)

Note that although the above discussion focussed on electrons as charge carriers, one expects that the current will change sign if the charge carriers are holes. This explains why the generated current flips sign along with ΔV : for positive bias, the charge carriers are electrons in the conduction band, whereas for negative bias, the charge carriers are holes in the valence band (a seamless transition is ensured by the fact that the bands are touching). Altogether, the proposed modeling strongly supports the hypothesis that the experimentally observed electric current is due to charge carriers being dragged by a phonon wind. Our model describes the momentum transfer from the liquid to the phonon distribution where an imbalance in the distribution develops. Scattering on the electron bath then results in an electronic current.

In conclusion we report the generation of a very large electronic current induced by the controlled motion of a liquid droplet at the surface of carbon nanomaterials. Our results suggest that the current generation is mediated by hydrodynamic momentum transfer from the liquid molecules to the phonons in the solid. Our specifically tailored system is particularly well suited to evidence the phonon-drag induced electronic current. Indeed, the combination of a local micrometric flow on strongly wrinkled graphene samples along with the choice of a very viscous and neutral liquid allows the phonon-drag as a direct momentum transfer to

dominate any other current generation mechanism. The versatility of our setup allows to tune the fluid velocity as well as the solid's electronic properties using the bias between the electrodes to fully characterize the phenomenon. Finally, all experimental results were rationalized with our new dedicated model of the phonon-drag. Our findings pave the way for the active control of fluid transport at the nanoscale by harnessing the interplay between fluid molecules and the collective excitation in the solid suggesting that novel nanofluidic functionalities can be proposed where a flow of fluid at the interface with tunable solid can be generated by externally excitable phonons or structural deformation waves. Further, the coupling of electronic and micro-fluidic currents bears the promise of ubiquitous and environmentally friendly energy production as demonstrated recently in titanium carbide MXene based transpiration-driven electrokinetic power generators [33].

ACKNOWLEDGEMENTS

L.B. acknowledges funding from the EU H2020 Framework Programme/ERC Advanced Grant agreement number 785911-Shadoks. A.S. acknowledges funding from FET-open ProID. The Flatiron Institute is a division of the Simons Foundation. B.C. acknowledges funding from a J.-P. Aguilar grant of the CFM Foundation, and thanks Olivier Parcollet for hosting him at the Flatiron Institute. B.R. acknowledges the Royal Society University Research Fellowship (URF/R1/180127) and European Research Council Starting Grant (agreement number 852674 - AngstroCAP). A.B. thanks Dr Ashok Keerthi for help in fabrication.

-
- [1] G. Gonella *et al.*, Water at charged interfaces, *Nature Rev. Chem.* **5** 466-485 (2021).
 - [2] N. Kavokine, R.R. Netz, L. Bocquet, Fluids at the nanoscale: from continuum to subcontinuum transport, *Ann. Rev. Fluid Mech.* **53** 377-410 (2021)
 - [3] P. Král and M. Shapiro, Nanotube electron drag in flowing liquids, *Physical Review Letters*, **86**, 131-134 (2014)
 - [4] S. Gosh, A. K. Sood and N. Kumar, Carbon Nanotube flow sensors, *Science*, **299**, 1042 (2003)
 - [5] A. Cohen, S. Gosh, A. K. Sood and N. Kumar, Carbon nanotubes provide a charge, *Science*, **300**, 1235-1236 (2003)
 - [6] B. N. J. Persson, U. Tartaglino, E. Tosatti and H. Ueba, Electronic friction and liquid flow-induced voltage in nanotubes, *Physical Review B*, **69**, 235410 (2004)
 - [7] Y. Zhao, L. Song, K. Deng, Z. Liu, Z. Zhang, Y. Yang, C. Wang, H. Yang, A. Jin, Q. Luo, C. Gu, S. Xie and L. Sun, Individual water-filled single-walled carbon nanotubes as hydroelectric power converters, *Advanced Materials*, **20**, 1772-1776 (2008)

- [8] J. Rabinowitz, C. Cohen, K. L. Shepard, An electrically actuated, carbon-nanotube-based biomimetic ion pump, *Nano Letters*, **20**, 1148-1153 (2020)
- [9] P. Dhiman, F. Yavari, X. Mi, H. Gullapalli, Y. Shi, P. M. Ajayan and N. Korathar, Harvesting energy from water flow over graphene, *Nano Letters*, **11**, 3123-3127 (2011)
- [10] J. Yin, Z. Zhang, X. Li, J. Zhou and W. Guo, Harvesting energy from water flow over graphene?, *Nano Letters*, **12**, 1736-1741 (2012)
- [11] S. H. Lee, Y. Jung, S. Kim and C.-S. Han, Flow-induced voltage generation in non-ionic liquids over monolayer graphene, *Applied Physics Letters*, **102**, 063116 (2013)
- [12] K. Kuriya, K. Ochiai, G. Kalita, M. Tanemura, A. Komiya, G. Kikugawa, T. Ohara, I. Yamashita, F. Ohuchi, M. Meyyappan, S. Samukawa, K. Washio and T. Okada, Output density quantification of electricity generation by flowing deionized water on graphene, *Applied Physics Letters*, **117**, 123905 (2020)
- [13] J. Yin, X. Li, J. Yu, Z. Zhang, J. Zhou and W. Guo, Generating electricity by moving a droplet of ionic liquid along graphene, *Nature Nanotechnology*, **9**, 378-383 (2014)
- [14] J. Park, S. Song, Y. Yang, S.-H. Kwon, E. Sim and Y. S. Kim, Identification of droplet-flow-induced electric energy on electrolyte-insulator-semiconductor structure, *Journal of the American Chemical Society*, **139**, 10968-10971 (2017)
- [15] J. Pei, J. Huang, Z. Huang and K. Liu, Liquid flow-induced electricity in carbon nanomaterials, *Sustainable Energy Fuels*, **3**, 599-610 (2019)
- [16] J. Comtet, A. Niguès, V. Kaiser, B. Coasne, L. Bocquet and A. Siria, Nanoscale capillary freezing of ionic liquids confined between metallic interfaces and the role of electronic screening, *Nature Materials*, **16**, 634-639 (2017)
- [17] , A. Schlaich, D. Jin, L. Bocquet, L., B. Coasne, Electronic screening using a virtual Thomas-Fermi fluid for predicting wetting and phase transitions of ionic liquids at metal surfaces, *Nature materials*, **21**, 237-245 (2022).
- [18] N. Kavokine, M.-L. Bocquet and L. Bocquet, Fluctuation-induced quantum friction in nanoscale water flows, *Nature*, **602**, 7895 (2022)
- [19] A. Fang, E. Dujardin and T. Ondarçuhu, Control of droplet size in liquid nanodispersing, *Nano Letters*, **6**, 2368-2374 (2006)
- [20] L. Fabié and T. Ondarçuhu, Writing with liquid using a nanodispenser: Spreading dynamics at the sub-micron scale, *Soft Matter*, **8**, 4995-5001 (2012)
- [21] <https://humminck.com>
- [22] Castro Neto, A. H., F. Guinea, N. M. R. Peres, K. S. Novoselov, and A. K. Geim The Electronic Properties of Graphene *Reviews of Modern Physics* **81**, (2009)
- [23] N. Liu, Z. Pan, L. Fu, C. Zhang, B. Dai and Z. Liu, The origin of wrinkles on transferred graphene, *Nano Research*, **4**, 996 (2011)
- [24] S. Deng and V. Berry, Wrinkled, rippled and crumpled graphene: An overview of formation mechanism, electronic properties and applications, *Materials Today*, **19**, 197-212 (2016)
- [25] B. Coquinet, L. Bocquet, N. Kavokine, Submitted, arXiv:2205.03250 (2022).
- [26] Nika, D. L. and Pokatilov, E. P. and Askerov, A. S. and Balandin, A. A., Phonon thermal conduction in graphene: Role of Umklapp and edge roughness scattering, *Phys. Rev. B*, **15**, 155413 (2009)
- [27] P.G. Klemens and D.F. Pedraza, Thermal conductivity of graphite in the basal plane, *Carbon*, **4**, 735-741, 32 (1994)
- [28] Ochoa, H. and Castro, Eduardo V. and Katsnelson, M. I. and Guinea, F. Temperature-dependent resistivity in bilayer graphene due to flexural phonons, *Phys. Rev. B*, **83**, 23 (2011)
- [29] Cong, X., Li, Q.-Q., Zhang, X., Lin, M.-L., Wu, J.-B., Liu, X.-L., Venezuela, P. and Tan, P.-H. Probing the Acoustic Phonon Dispersion and Sound Velocity of Graphene by Raman Spectroscopy, *Carbon*, **149**, (2019)
- [30] A. Gruneis, C. Attaccalite, L. Wirtz, H. Shiozawa, R. Saito, T. Pichler, A. Rubio, Tight-binding description of the quasiparticle dispersion of graphite and few-layer graphene, *Physical Review B*, **78**, 1-16 (2008)
- [31] F. Guinea, M. I. Katsnelson, M. A. H. Vozmediano, Midgap states and charge inhomogeneities in corrugated graphene, *Physical Review B*, **77**, 1-8 (2008)
- [32] J. C. Charlier, J. P. Michenaud, P. Lambin, Tight-binding density of electronic states of pregraphitic carbon, *Physical Review B*, **46**, 4540-4543 (1992)
- [33] Bae, Jaehyeong, Min Soo Kim, Taegon Oh, Bong Lim Suh, Tae Gwang Yun, Seungjun Lee, Kahyun Hur, Yury Gogotsi, Chong Min Koo, and Il-Doo Kim Towards Watt-Scale Hydroelectric Energy Harvesting by $\text{Ti}_3\text{C}_2\text{T}_x$ -Based Transpiration-Driven Electrokinetic Power Generators, *Energy and Environmental Science*, **15** (2022)

Supplementary Material for: Strong electronic winds blowing under liquid flows on carbon surfaces

Alice Marcotte^{†,1} Mathieu Lizee^{†,1} Baptiste Coquinot,^{1,2} Nikita Kavokine,² Karen Sobnath,³ Clément Barraud,³ Ankit Bhardwaj,^{4,5} Boya Radha,^{4,5} Antoine Niguès,¹ Lydéric Bocquet,¹ and Alessandro Siria¹

¹*Laboratoire de Physique de l'École Normale Supérieure,
ENS, Université PSL, CNRS, 3 Sorbonne Université,
Université Paris Cité, 75005 Paris, France*

²*Center for Computational Quantum Physics, Flatiron Institute, New York, USA*

³*Université Paris Cité, Laboratoire Matériaux et Phénomènes Quantiques, CNRS, F-75013 Paris, France*

⁴*National Graphene Institute, The University of Manchester, UK*

⁵*Department of Physics and Astronomy, The University of Manchester, UK*

CONTENTS

I. Graphene-based device's micro-fabrication	1
A. Transferred samples	1
B. Un-transferred samples	1
II. Droplet motion-induced current generation	2
A. Controls	4
B. Wrinkles are current amplifiers	4
III. Theoretical model	6
A. Electron drag: Phonon drag vs. Coulomb drag	6
B. Electronic state and electric current	8
C. Model for the solid	9
References	9

I. GRAPHENE-BASED DEVICE'S MICRO-FABRICATION

A. Transferred samples

The HOPG crystals are purchased from HQ Graphene. Each bulk crystal is mechanically exfoliated and flakes are first randomly deposited on separate 280 nm-thick Si/SiO₂ substrates. The thickness of the SiO₂ layer is chosen to maximize the optical contrast [2]. Graphene flakes are then carefully selected for their thickness (ranging from 1 nm to 70 nm), homogeneity and size ($> 15 \mu\text{m}$). h-BN flakes of thicknesses between 7 and 15 nm are chosen. In the case of graphite/SiO₂ devices, the graphene flakes are transferred thanks to the

“hot pick-up” technique [3, 4] in a 100 x 100 μm^2 area in the middle of a 2x2 mm^2 pre-patterned substrate with Au electrodes. In the case of h-BN supported graphene devices, h-BN and graphene flakes are first stacked and then transferred on the pre-patterned devices using the same technique. The devices are then fabricated by defining two parallel electrical contacts over the graphene flake by e-beam lithography using a double layered PMMA process: a 50 K lower layer of PMMA and a 950 K upper layer of PMMA both spin-coated at 4000 RPM. The spacing between the two contacts is set to at least 10 μm for the AFM experiment. The metallic contacts are subsequently deposited under high vacuum (a few 10⁻⁷ mBar) by e-beam evaporation. 5 nm of Ti covered by 45 nm (or 95 nm) of Au are deposited at very low evaporation rates (0.1 nm/s). The last fabrication step is a lift-off process in which the remaining resist is dissolved in an acetone bath for 20 min. The samples are finally rinsed into isopropanol for 2 min. This fabrication method involves a transfer of the graphite flake and thus yields a high density of wrinkles on thinner flakes as measured by AFM (see Figure S1 **a,b**). As the viscous-flow induced current did not show any clear difference between SiO₂ and hBN supported devices, we disregard this detail in the following.

B. Un-transferred samples

As discussed in the text, wrinkles have a strong influence on viscous flow driven current generation at the carbon surface. To assess the role of wrinkles in current generation, we used a transfer-free fabrication technique to prepare flat graphite samples. We evaporated gold electrodes on the SiO₂ substrate where the graphite was exfoliated in the first place and thus ob-

[†] These authors contributed equally to this work

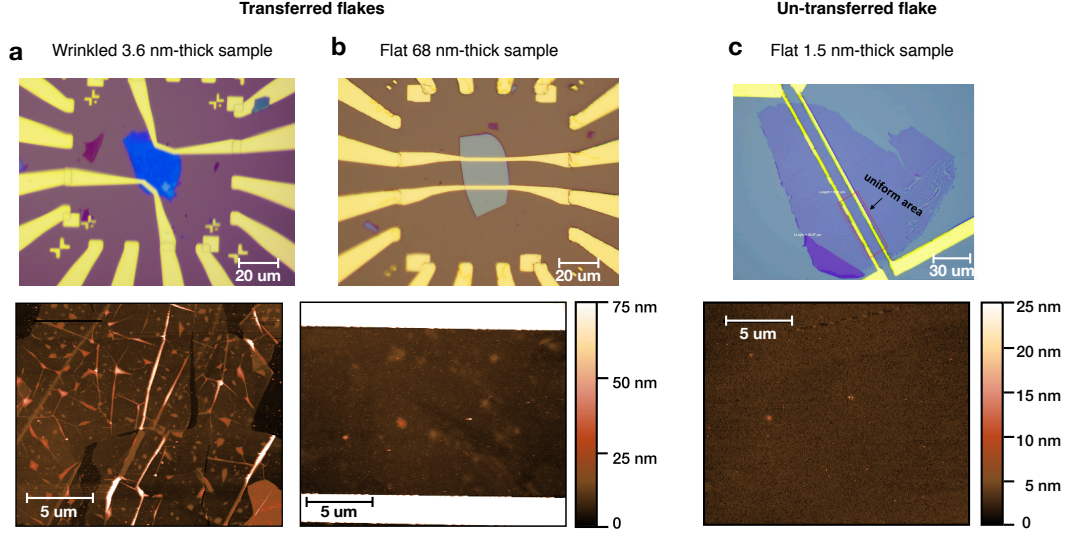


Figure S1: Samples prepared by the two alternative techniques. On **a** and **b**, we show optical and AFM images of transferred samples. The few nanometers thick samples like **a** show a high wrinkle density while the thicker ones (see **b**) are very flat. On **c**, we show an un-transferred sample which displays negligible wrinkle density even for very low thickness (1.5 nm).

tained wrinkle-free samples which can be compared to high wrinkle-density samples of the same thickness obtained when transferring the flakes before evaporating the contacts (see Figure S1 c).

II. DROPLET MOTION-INDUCED CURRENT GENERATION

a. Micro-pipette AFM preparation The capillary tip is obtained by locally heating and simultaneously pulling a 10 cm long quartz capillary of inner diameter 0.5 mm and outer diameter 1 mm (World Precision Instruments), with a Sutter Instruments P-2000 pipette puller. The capillary tube is separated into two pipettes. Each of them has one cylindrical end, and one conical taper on the other end with a tip outer diameter of 500 nm, that can be varied by tuning the pulling parameters.

The pipette is then filled with ionic liquid (Bmim-PF6 of high purity from Merck) or with neutral silicon oil (Polyphenyl-methylsiloxane, 100 mPa.s, from Sigma Aldrich). This step is greatly facilitated by the inner filament in the pipette, which enhances the capillary filling of the tip. Once the pipette is filled, its very extremity is glued with epoxy glue on the lateral side of a millimetric quartz tuning fork prong. With a diamond tip, the largest part of the capillary is then cut free from its extremity and from the tuning fork. These steps are summa-

rized by Figure S2a.

Finally, the tuning fork and its probe are examined under Scanning Electron Microscopy, to measure the outer diameter of the pipette extremity and to make sure the previous fabrication steps did not damage the tip, see Figure S2b.

b. Liquid droplet creation and control All our experiments are conducted under ambient conditions. To deposit a very small and controlled amount of liquid on the graphite, and to put the deposited droplet in motion over the sample while keeping constant the degree of squeezing of the droplet, we use the tuning fork as an autosensitive Atomic Force Microscope (AFM) mechanical oscillator. The tuning fork is excited *via* a piezo-dither at its resonance frequency f_0 in the normal mode ($f_0 \approx 32$ kHz), while the amplitude and phase shift of the tuning fork oscillations with regards to the excitation AC voltage are obtained from the piezoelectric current flowing through the tuning fork electrodes. Our home-made AFM is used in frequency-modulation mode : a Phase Lock Loop (PLL) ensures that the tuning fork is systematically excited at its resonant frequency. Furthermore, a PID servo loop maintains a constant oscillation amplitude at resonance by tuning the excitation voltage. Interactions with the substrate are detected by the change in the resonance frequency and in the excitation amplitude. As shown on Figure S2c, we use a camera to perform the coarse approach of the AFM

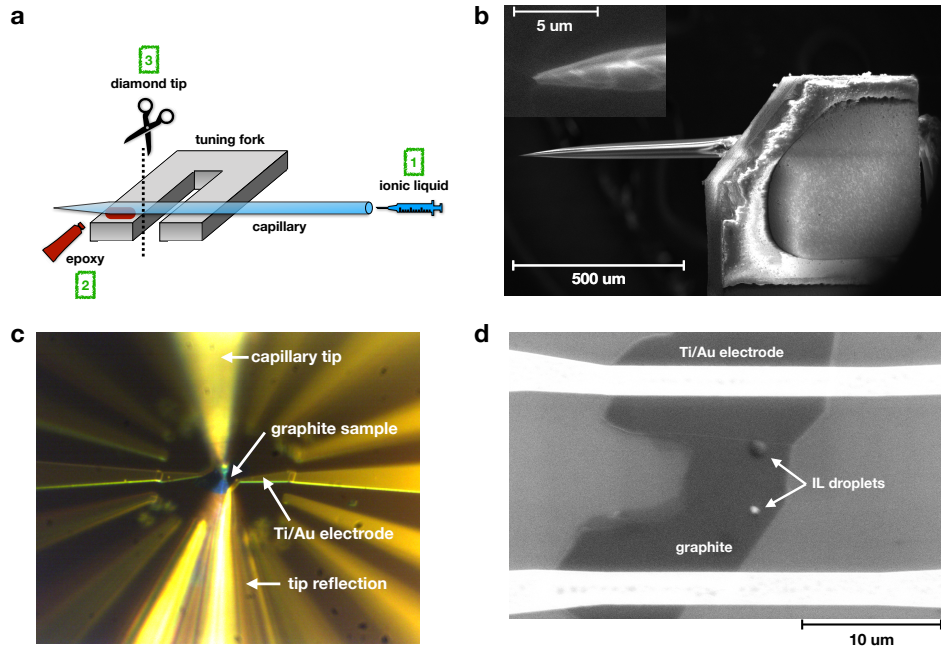


Figure S2: **a** Steps for the preparation of the tuning fork and its probe: Firstly, the pipette is filled with liquid. Then, it is glued with epoxy on the side of one tuning fork prong. Finally, the cylindrical part of the capillary is cut free from its extremity and from the tuning fork with a diamond tip. **b** Scanning Electron Microscopy images of the lower prong of a millimetric tuning-fork, and of the extremity of the pipette glued on it (*inset*). **c** In-situ microscope view of the graphite sample connected by two Ti/Au electrodes, while the capillary tip is moving an ionic liquid droplet on the substrate. **d** Post-experiment Scanning Electron Microscopy image of a graphite sample. Two roughly spherical ionic liquid droplets remain on the flake.

tip and we monitor the gentle approach *via* the PLL to detect contact with the substrate and the formation of the capillary bridge, and to ensure a constant contact stiffness (frequency-shift) during the droplet motion on the sample.

c. Current measurement The sample's motion is controlled by a XYZ-scanner. Once the droplet is formed on the graphite sample, the X and Y position of the scanner are modulated by a Lock-In at the chosen amplitude (between 100 nm and a few microns) and at the chosen frequency (between 100 mHz and a few Hertz) while the electric current flowing through the electrodes on the graphite sample is demodulated at the droplet oscillation frequency. The direction of the droplet oscillation can be chosen, this allows to vary the angle between the droplet's motion axis and the inter-electrodes axis. Prior to any measure-

ment of the generated current dependency on the modulation amplitude, we search for the scan angle leading to an alternating current with maximal amplitude, for a given frequency and amplitude of oscillations, around a given central position. Then we measure around the same central position and along the optimal axis, how the current amplitude varies with the oscillation amplitude at a given frequency, and how it depends on the bias voltage ΔV .

d. Shape-preserving motion of the droplet To make sure the reported phenomena are not related to the deformation of the interaction surface between the liquid droplet and graphite, we imaged the samples after the current measurements under Scanning Electron Microscopy. As shown on Figure S2d, the remaining droplets display a roughly spherical shape, which confirms that scanning of the sam-

ple with the capillary tip does not result in the deposition of a liquid line, but instead, in the sliding of a hemispherical droplet over graphite.

e. Data processing To extract the droplet-motion induced current, we record the generated current as a function of time for at least 50 periods of droplet oscillations. The generated current amplitude is defined as the Fourier component of current corresponding to the droplet oscillation frequency (see Figure S3).

A. Controls

To make sure that the measured current is indeed related to the viscous flow of liquid on graphite, we performed extensive controls which we detail here. We measure the current in various experimental configurations and show that the motion of a viscous droplet on top of the graphite flake is necessary to measure a non-zero current. Finally, we demonstrate the predominance of viscosity over charge or polarity of the liquid to convince the reader that the viscous friction of liquid on graphite is at the origin of the motion induced current.

a. Pipette above the droplet We first checked that no current can be generated if the pipette is not in contact with the liquid droplet but is slightly above instead (see Figure ??). In this configuration, a liquid droplet is deposited on graphite and the pipette is subsequently retracted and brought a few μm above the liquid. Thus, during the oscillation, no motion is induced between the droplet and the sample. As shown on Figure S4, we do not measure any motion induced current in this situation.

b. On SiO_2 We also checked that no current can be generated if the droplet moves over the SiO_2 surface comprised between the electrodes, see Figure S4b. Finally, these controls show unambiguously that current generation requires the droplet to slide on the graphite surface.

c. With a neutral and apolar silicon oil droplet Finally, we performed an additional control to confirm a mechanism relying on momentum transfer-mediated current generation by using neutral and apolar silicon oil (Polyphenyl-methylsiloxane) instead of ionic liquid, with similar viscosity (0.1 Pa.s instead of 0.3 Pa.s for the ionic liquid). As evidenced by Figure S5, the current generation is also possible in this configuration with induced currents of the same order of magnitude than with ionic liquid. This confirms that the motion-induced current is caused by a momentum transfer which dominates any electrostatic contribution.

d. Frequency dependency of generated current The current density displays a puzzling dependency on the oscillation frequency: While at a given frequency, the current amplitude scales linearly with the oscillation amplitude/velocity, when fixing the oscillation amplitude, the current amplitude decreases with frequency. Thus, the moving droplet-graphite system behaves as a low-pass filter with a cut-off frequency in the order of 1 Hz, see Figure S6. This dependency is rather unexpected since such long time-scales cannot come from the solid state where electrons and phonons relax much faster. Thus, we attribute this behavior to a thin wetting film spread on the droplet trajectory, which would reduce the effective friction (and therefore the generated current) and could have such slow dynamics. In this scenario, increasing the frequency is not equivalent to increasing the oscillation amplitude.

B. Wrinkles are current amplifiers

As discussed previously, our sample fabrication techniques allow us to produce graphite flakes of desired thickness with either a high wrinkle density (transferred flakes) or a very flat surface showing negligible roughness (un-transferred flakes). We were therefore able to study the dependency of generated current on both thickness and wrinkle density independently. On Figure S7 a, we illustrate the thickness-dependency of the current induced by droplet oscillations of $1 \mu\text{m}\cdot\text{s}^{-1}$ for both transferred (diamonds) and un-transferred (circles) graphite flakes. Our experiments reveal that for transferred samples, the thinner the graphite flake, the more efficient the current generation. Primarily, we observe a transition for the current generation around 10 nm in thickness: for flakes thicker than 10 nm, no current generation is possible, while current can be induced at the surface of flakes thinner than 10 nm. On the other hand, we report no generated current for flat un-transferred samples down to single nanometer thickness.

Our results demonstrate that wrinkles are a prerequisite to the viscous flow induced current generation. Another experimental evidence of the predominant role played by the wrinkles resides in the strong spatial anisotropy of the generated current (current depends on oscillation direction). As shown in Figure S8, the directional dependency depends strongly on the position on the sample surface. This variability is linked to the random distribution in height, position and direction of the wrinkles over the

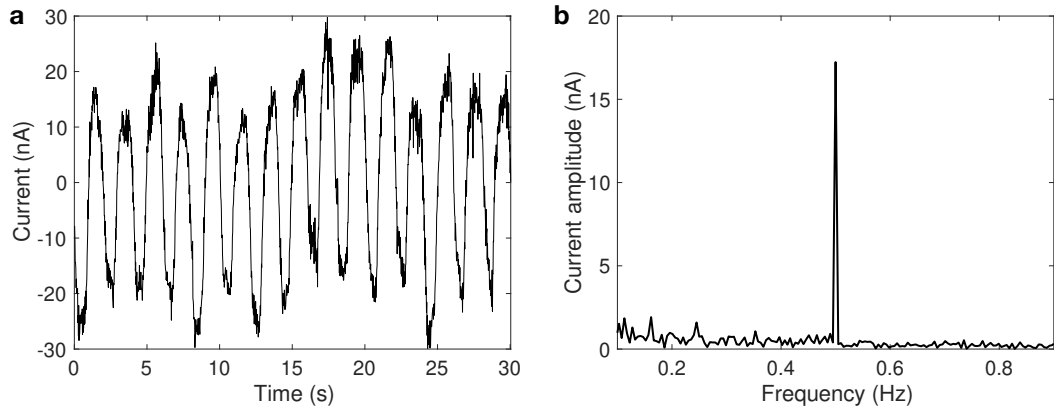


Figure S3: **a**, Current as a function of time, for droplet oscillations of $2 \mu\text{m}$ amplitude and 0.5 Hz frequency. **b**, Current spectrum as a function of frequency. The spectrum displays a peak at the droplet oscillation frequency (0.5 Hz). The peak maximal value is defined as the generated current amplitude.

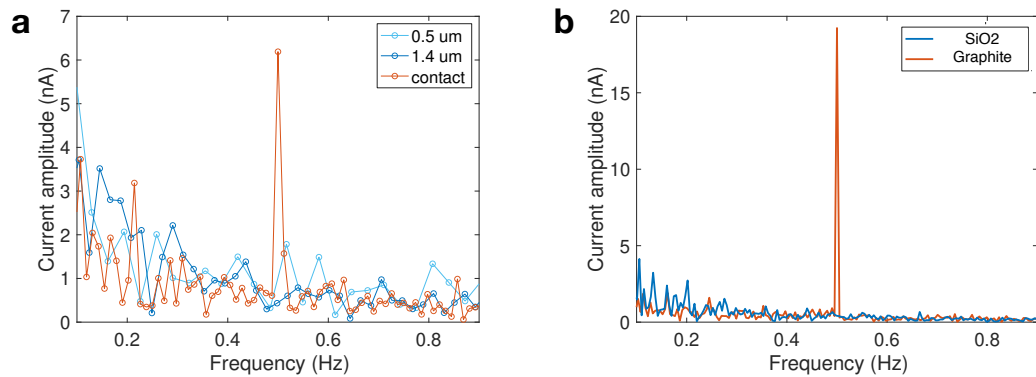


Figure S4: **a** Current spectrum (nA) as a function of the frequency (Hz) while the capillary tip moves at $5 \mu\text{m}$ and 0.5 Hz in amplitude and frequency, $0.5 \mu\text{m}$ (clear blue curve) and $1.4 \mu\text{m}$ (dark blue curve) above the graphite, and in contact with the graphite *via* the ionic liquid droplet (red curve). **b** Current spectrum (nA) as a function of the frequency (Hz) for a droplet motion of $2 \mu\text{m}$ amplitude and 0.5 Hz frequency, on graphite (red curve) and on SiO₂ (blue curve).

graphite surface.

a. Raman spectroscopy To strengthen our claim that wrinkles are folded graphene structures that increase liquid friction and thus motion-induced current by a mere geometrical effect, we perform Raman spectroscopy on one transferred graphite sample and demonstrate that wrinkles show a ratio of D-peak intensity over G-peak intensity of the same order as flatter regions and that they show the usual spectroscopic properties of graphite samples. The measurements are presented on Figure S9. On **a**, we show the AFM scan of a transferred sample. On this sample, the transfer process has torn apart a top layer of graphite which is therefore showing wrinkles on top of the un-

derlying graphite crystal (dark region). We use this particular sample to study the structural properties of wrinkles compared to a flat crystal. On **b**, we display a typical Raman spectrum measured with a 532 nm laser on this sample. Furthermore, on **c**, we display the G peak intensity map, revealing the in-homogeneity of thickness in the folded regions (higher G peak means thicker region). Finally, on **d**, we show the ratio of D-peak over G-peak intensity. This shows that wrinkles and folded regions are by no means defects. This analysis strengthens our theoretical treatment of wrinkles and folded regions as graphite or graphene with an enhanced corrugation.

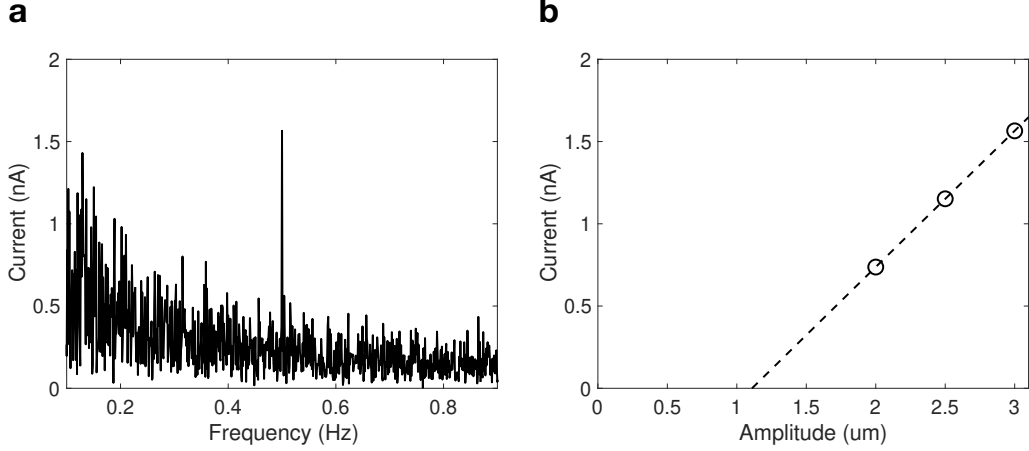


Figure S5: **a** Current spectrum (nA) as a function of the frequency (Hz) for a micrometric silicone oil droplet oscillating at 0.5 Hz and 3 μm in amplitude on the graphite sample. **b** Generated current amplitude as a function of the silicon oil droplet oscillation amplitude, at 0.5 Hz. The circles are the experimental data, while the dotted line is the best linear fit. All these measurements are taken at a bias voltage $\Delta V = 0\text{mV}$.

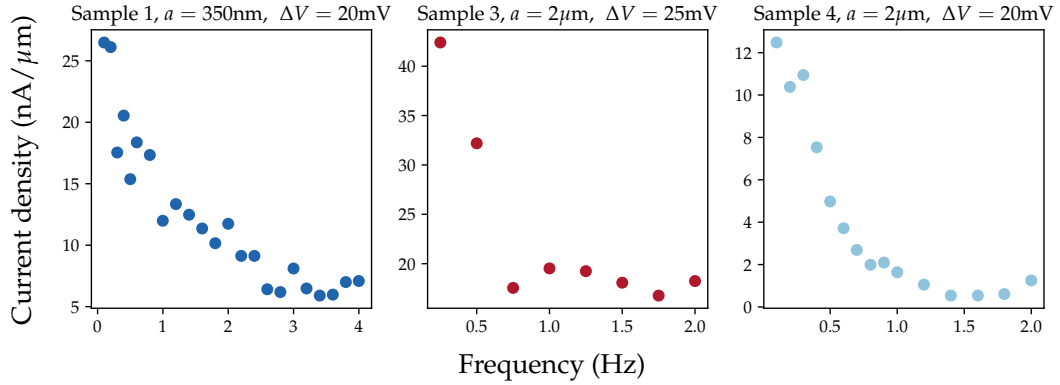


Figure S6: Generated current amplitude as a function of the oscillation frequency. We show the dependency measured on three different samples (corresponding to those described in the main text) namely samples 1, 3 and 4. The oscillation amplitude and bias are given above each plot.

III. THEORETICAL MODEL

A. Electron drag: Phonon drag vs. Coulomb drag

The electrons are dragged both by phonon drag and Coulomb drag. These two phenomena have recently been studied formally in the Keldysh framework by Coquinot *et al.* [5]. According to the authors, they can be treated similarly as bosons, either phonons or liquid fluctuations of the drop (called *hydrons*), interacting with electrons. The liquid fluctuations drag the electrons at the interfacial liquid velocity

v_ℓ and $v_\ell \ll v_{\text{drop}}$ as the slip length is small compared with the drop height. On the other side, the phonons drag the electrons at the effective velocity \mathbf{v}_{eff} calculated in the main text: $v_{\text{eff}} \approx 9 \cdot 10^4 \times (1+W) \times v_{\text{drop}}$. In the stationary regime, the electrons reach an electronic velocity

$$\mathbf{v}_e(\mathbf{q}) = \frac{\tau_{\mathbf{q}}}{\tau_{\mathbf{q}}^{e/\text{ph}}} \mathbf{v}_{\text{eff}} + \frac{\tau_{\mathbf{q}}}{\tau_{\mathbf{q}}^{e/\text{h}}} \mathbf{v}_\ell \approx \frac{\tau_{\mathbf{q}}}{\tau_{\mathbf{q}}^{e/\text{ph}}} \mathbf{v}_{\text{eff}} \quad (1)$$

Here $\tau^{e/\text{b}}$ is the electron-boson interaction time and τ is the total electronic scattering time ($1/\tau = 1/\tau^{e/\text{ph}} + 1/\tau^{e/\text{h}}$). Therefore, the electronic velocity is the convex combination of

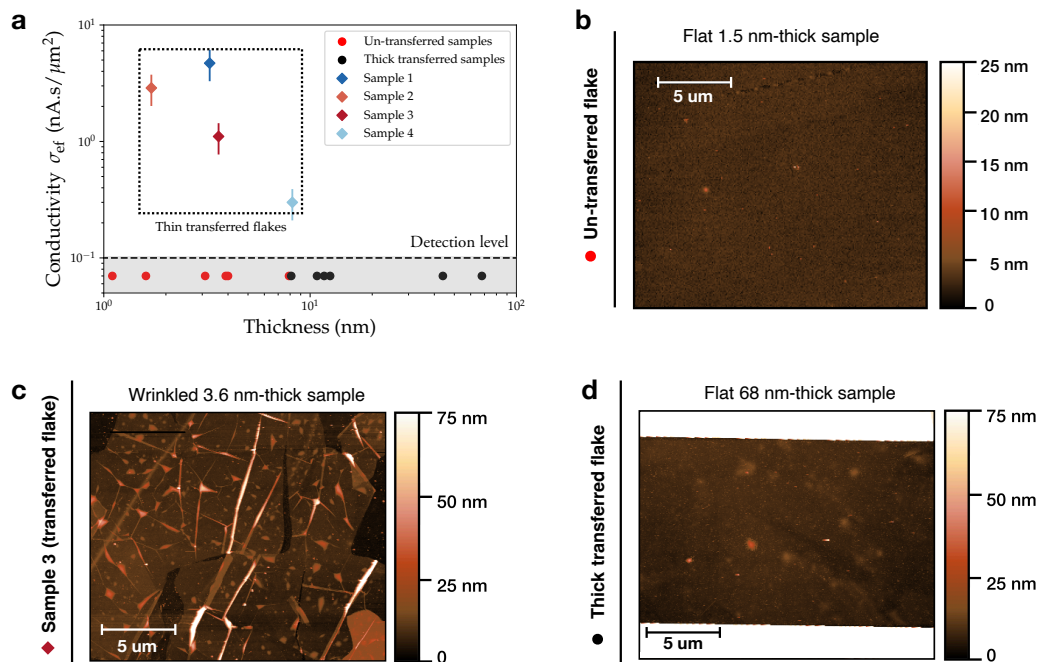


Figure S7: **a** Semilog plot of the normalized generated current given in $nA/\mu\text{m}\cdot\text{s}^{-1}$, as a function of the flake thickness. **b** AFM image of a flat 1.5 nm-thick sample (un-transferred). **c** AFM image of a current generating wrinkled 3.6 nm-thick sample (transferred). **d** AFM image of a flat 68 nm-thick sample (transferred). No wrinkles are induced and thus no current is measured. On samples thicker than 10 nm, no wrinkles are observed and the droplet oscillations do not result in the generation of a measurable current. Similarly, on the thinner samples, current generation requires the wrinkles.

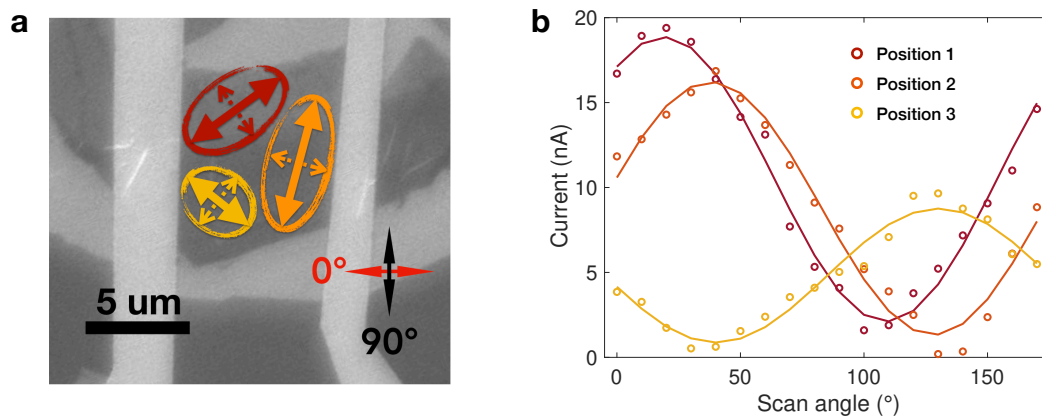


Figure S8: **a** Scanning electron microscopy image of a graphite sample. Current is generated by droplet motion of constant amplitude and frequency, along axis forming tilted with respect to the electrode axis by the 'scan angle'. We stress that **a** is a schematic and that our in-situ microscope does not allow such a fine positioning. Here, as detailed on **b**, we merely show that the angular dependency of the generated current also depends of the region of the sample that we are scanning. **b** Generated current (nA) as a function of the scan angle ($^\circ$) of droplet motion (at 0.5 Hz frequency and 1 μm amplitude), around various central positions. As expected, the current is a 180° -periodic function of the oscillations angle, but interestingly the phase depends on the central positions of the oscillations. For each location, the experimental points are pictured by circles, while the solid line is the best sinusoidal fit.

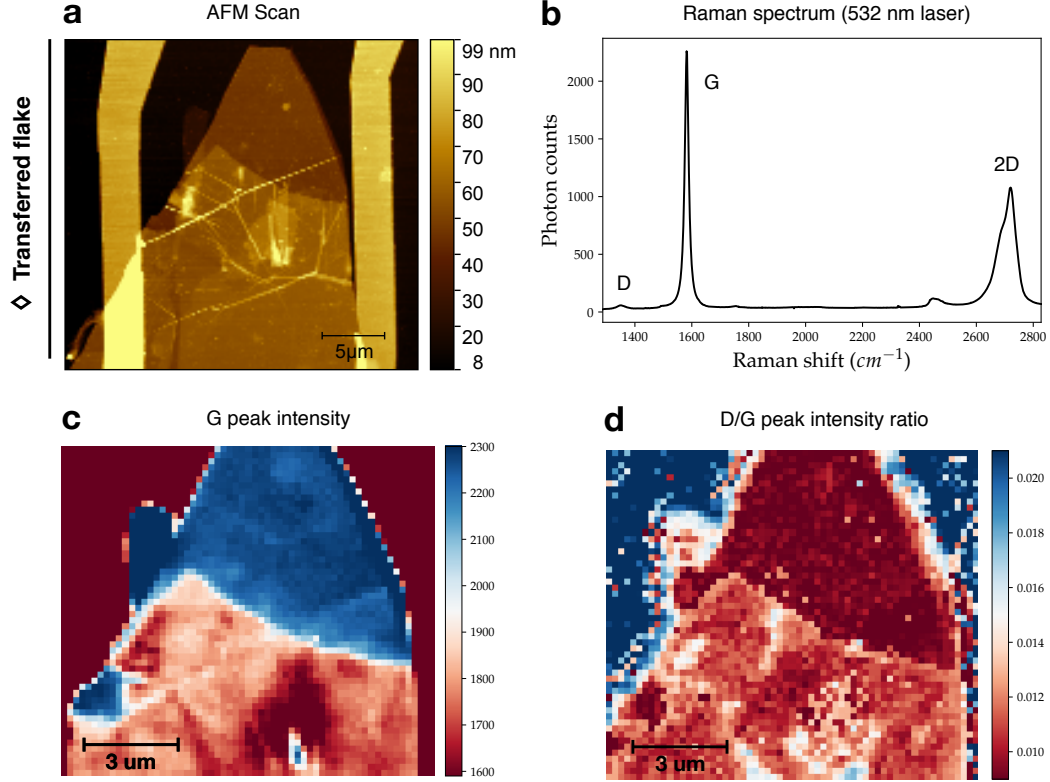


Figure S9: A transferred graphite sample shows wrinkles as discussed above and shown by AFM imaging in **a**. On **b**, a typical Raman spectrum is shown. The Raman G-peak intensity is displayed on **c** and is stronger in the thicker regions. On **d**, the intensity ratio between the D and G peak is displayed. The low value (1%) of this ratio indicate a very low level of defects. Moreover, wrinkles, as opposed to flake edges do not display any local D-peak enhancement. This indicates that wrinkles are indeed folded graphene structures and neither pollution nor defects.

the phonon effective velocity and the interfacial liquid velocity. In practice, in our model, $\tau_{\mathbf{q}}/\tau_{\mathbf{q}}^{e/ph} \approx 1/2$. In Eq. (1) the first term describes the effect of the phonon drag while the second term describes the effect of the Coulomb drag. Let us notice that the Coulomb drag effect reduces the electronic velocity: it then contributes negatively to the electric current generation.

B. Electronic state and electric current

In stationary regime, the electronic distribution of band dispersion $\epsilon_{\mathbf{q}}$ is shifted according to $\epsilon_{\mathbf{q}} \mapsto \epsilon_{\mathbf{q}} - \hbar\mathbf{q} \cdot \mathbf{v}_e$. Therefore, the distribution will be filled above the doping level ϵ_F in the velocity direction, and below in the opposition direction. Since the solid is 2D, the angle integration will provide a trigonometric factor $1/2$. The distribution is not at zero tempera-

ture, thus the energies close to the doping level up to the thermal energy matter. Moreover, the interaction broadens the electronic distribution around the band structure. According to [5], in stationary regime, the electronic distribution reads

$$n_e(\mathbf{q}, \omega) = \frac{2\tau/\hbar \times n_F(\omega - \mathbf{q} \cdot \mathbf{v}_e(q))}{1 + (\frac{\tau}{\hbar})^2 (\hbar\omega + \epsilon_{\mathbf{q}} - \epsilon_F)^2} \quad (2)$$

where n_F is the Fermi-Dirac distribution and τ is the electronic scattering time. Therefore, taking into account the spin degeneracy, the authors of [5] predict an electric current

$$\langle \mathbf{j} \rangle = 2e \int d\epsilon d\omega \frac{(\nabla_{\mathbf{q}} \epsilon_{\mathbf{q}})_{\epsilon} N(\epsilon) \hbar q_{\epsilon} \mathbf{v}_e}{4k_B T \text{ch}^2 \left[\frac{\hbar\omega + \epsilon - \epsilon_F}{2k_B T} \right]} 1 + \tau_{\epsilon}^2 \omega^2} \quad (3)$$

where ϵ describes the band energy levels. Here, $(\nabla_{\mathbf{q}} \epsilon_{\mathbf{q}})_{\epsilon}$ is the band velocity and q_{ϵ} the momentum both at the band energy level ϵ . Going to

the limit of small interaction and low temperature $\hbar\tau^{-1} \ll k_B T \ll \epsilon_F$, we recover Eq. (2) of the main text.

C. Model for the solid

Using a linear dispersion relation to describe graphene yields an energy-dependent density of states. When the doping vanishes we expect no current because of the electron-hole symmetry. For large dopings $\epsilon_F \gg k_B T$, only one band matters and the electric current writes $\langle \mathbf{j} \rangle \approx e \mathbf{v}_e \epsilon_F^2 / (\hbar v_F)^2$, where $v_F = 10^6$ m/s is the Fermi velocity of graphene. The current is then quadratic in doping, which is consistent with the total average charge of the charge carriers. At smaller doping, temperature effects appear

and a linear regime exists when $\epsilon_F \ll k_B T$. Experimentally, most measurements are in this regime but one may expect nonlinear effects for the higher bias voltage applied. As no such effect is measured in practice the relevance of this model may be questioned. Moreover, numerical applications lead to an electric current 1 order of magnitude smaller than experimentally measured.

To describe more precisely our samples, we used a model for multi-layer graphene made of two independent parabolic bands with effective mass m [6–8]: $\epsilon_{\mathbf{q}} = \hbar^2 q^2 / 2m$. In particular, the density of states does not depend on the doping, which is key to get a linear dependence for the current. The predicted current is then $\langle \mathbf{j} \rangle \approx 2e v_e m \epsilon_F / \hbar^2$ from which is deduced Eq. (4) of the main text.

-
- [1] J. K. Moon, J. Jeong, D. Lee and H. K. Pak, Electrical power generation by mechanically modulating electrical double layers, *Nature communications*, **4**, 1487 (2013)
- [2] Roddaro, S., Pingue, P., Piazza, V., Pellegrini, V. and Beltram, F. The Optical Visibility of Graphene: Interference Colors of Ultrathin Graphite on SiO₂ *Nano Letters* (2007)
- [3] Pizzocchero, F. et al. The hot pick-up technique for batch assembly of van der Waals heterostructures *Nature communications*, 11894 (2016)
- [4] Rastikian, J. et al. High performance room temperature p-type injection in few-layered tungsten diselenide films from cobalt and palladium contacts *Material Research Express* (2019).
- [5] B. Coquinot, L. Bocquet, N. Kavokine, Submitted, arXiv:2205.03250 (2022).
- [6] A. Gruneis, C. Attaccalite, L. Wirtz, H. Shiozawa, R. Saito, T. Pichler, A. Rubio, Tight-binding description of the quasiparticle dispersion of graphite and few-layer graphene, *Physical Review B*, **78**, 1–16 (2008)
- [7] F. Guinea, M. I. Katsnelson, M. A. H. Vozmediano, Midgap states and charge inhomogeneities in corrugated graphene, *Physical Review B*, **77**, 1–8 (2008)
- [8] J. C. Charlier, J. P. Michenaud, P. Lambin, Tight-binding density of electronic states of pregraphitic carbon, *Physical Review B*, **46**, 4540–4543 (1992)